Journal of Nuclear Materials 614 (2025) 155913

Contents lists available at ScienceDirect

Journal of Nuclear Materials

journal homepage: www.elsevier.com/locate/jnucmat

Heat-treated additively manufactured and wrought 316L steels display a comparable response to ion irradiation

Benjamin M. Jenkins [a,*], Solène Rouland [a], Auriane Etienne [a], Anna Kareer [b], Jack Haley [c], Cristelle Pareige [a], Philippe Pareige [a], Bertrand Radiguet [a]

[a] CNRS, INSA Rouen Normandie, Groupe de Physique des Matériaux UMR 6634, Univ Rouen Normandie, F-76000 Rouen, France
[b] Department of Materials, University of Oxford, Parks Road, Oxford, OX1 3PH, United Kingdom
[c] UKAEA, Culham Campus, Abingdon, Oxfordshire OX14 3DB, United Kingdom

GRAPHICAL ABSTRACT

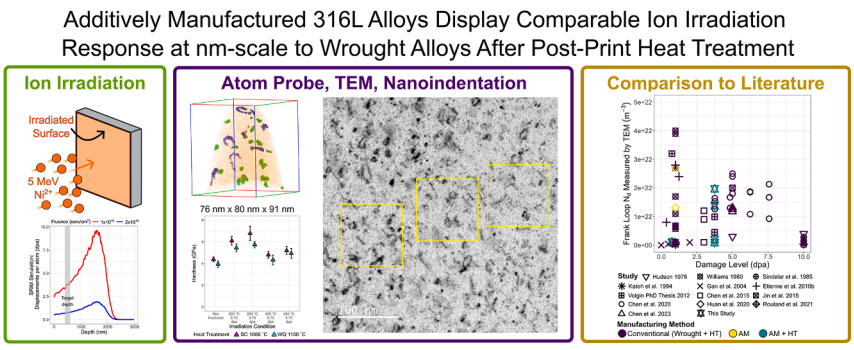

ARTICLE INFO

Keywords:
Additive Manufacturing
Ion irradiation
Austenitic stainless steel
Atom probe tomography (APT)
Transmission electron microscopy (TEM)

ABSTRACT

Additive manufacturing produces metallic components with inhomogeneous microstructures. This inhomogeneity can negatively impact mechanical properties and in-service performance. Applying post-printing heat treatments can reduce microstructural inhomogeneity but a validation of alloy performance, under specific operational environments is still required.

316L stainless steels are used for a variety of components in nuclear power plants. They are exposed to irradiation at elevated temperature during service, which alters the microstructure and mechanical properties. To validate the implementation of additively manufactured 316L components in environments where they are exposed to irradiation, it is necessary to ensure that additively manufactured components will display comparable behaviour under irradiation to their wrought counterparts.

In this study we use atom probe tomography, transmission electron microscopy, and nanoindentation to investigate the response of additively manufactured 316L alloys, produced by laser powder bed fusion, exposed to ion irradiation. Our results, when compared to published data on wrought 316L alloys, demonstrate that performing post-printing heat treatments at 1066 °C and 1150 °C leads to 316L alloys that display a comparable response to ion irradiation when compared to conventionally manufactured 316L specimens.

* Corresponding author.
E-mail address: benjamin.jenkins@univ-rouen.fr (B.M. Jenkins).

https://doi.org/10.1016/j.jnucmat.2025.155913
Received 7 March 2025; Received in revised form 23 April 2025; Accepted 20 May 2025
Available online 22 May 2025

1. Introduction

Additive Manufacturing (AM) is a potentially disruptive technology that offers the ability to create net-shape components, reduce waste, and provide economic savings [1–3]. Another advantage of AM is that it may help reduce the long lead times that are currently associated with producing complex-shaped components via conventional production routes [4]. The ability to use AM to rapidly prototype novel components for advanced nuclear power plant reactor designs and also to produce replacement parts that are no longer in production is desirable for the nuclear industry. However, the evolution of AM alloys' microstructures and properties when exposed to in-service conditions, compared to their wrought counterparts, is currently not well understood. This has safety implications for the nuclear industry, where strict safety standards must be met before regulatory approval is obtained.

One of the key degradation mechanisms that components experience during service in nuclear power plants is radiation damage from the high energy neutrons produced during the fission reaction [5–7]. However, due to the high cost, extended timelines required to conduct experiments, and the difficulty in handling the radioactive materials that are produced, it is common practice to perform surrogate irradiation campaigns using accelerated ions [8]. Whilst there are difficulties and challenges associated with using ion irradiation data to predict how materials will respond to neutron irradiation, ion irradiation studies enable us to compare how dissimilar materials respond to similar irradiation environments [8].

316L is a stainless-steel that is widely used in the nuclear industry and may be produced by AM. 316L steels have good creep and corrosion resistance at elevated temperature and are extensively used for reactor internals in light water nuclear power plants [9,10]. The irradiation response of wrought 316L steels' microstructures has been fairly well characterised [11–20]. Previous ion irradiation studies on wrought 316L steels have primarily used transmission electron (TEM) to study dislocation loop evolution (size, number density) with dose and/or irradiation temperature [11–13], whilst atom probe tomography (APT) has been used to characterise solute segregation [15,21,22]; this research has revealed that solute cluster formation is due to the inverse Kirkendall effect leading to Ni and Cr segregation, whilst Si diffuses via an interstitial mechanism [22,23].

Despite the large amount of work on wrought 316L, literature on the irradiation response of solution-annealed AM 316L is currently limited and requires further investigation. Most studies on the irradiation response of AM 316L focus on samples with an as-printed microstructure [24–29], which is unlikely to be the microstructure that is present in engineering components during service. Whilst some studies have looked at the irradiation response of AM 316L after undergoing a post-printing heat treatment [30], they contain little-to-no characterisation of microstructural features with TEM or APT. There is, therefore, a gap in our knowledge as to whether the microstructure of solution-annealed AM 316L will develop in the same way as that of wrought 316L when exposed to irradiation, and whether it is the same mechanisms that control solute segregation. This presents a challenge in gaining regulatory approval for the deployment of AM 316L in components exposed to irradiation during service.

In this article, we present results on the ion irradiation response of additively manufactured 316L specimens, produced by laser powder bed fusion (LPBF), that have undergone two different post-printing heat treatments. Samples from each alloy were exposed to four different irradiation conditions, enabling the role of varying irradiation dose and temperature to be investigated. Microstructural characterisation of the irradiated microstructure was performed with atom probe tomography (APT) and transmission electron microscopy (TEM). Solute cluster formation, dislocation evolution, and elemental segregation was characterised. Nanoindentation was used to investigate how the mechanical properties of these samples evolved under irradiation. We compare our results to those previously published in the literature, which reveals a comparable response to ion irradiation between heat-treated LPBF 316L and 316L alloys produced via conventional processes. These results are promising and indicate that AM 316L may be used in more components within the nuclear industry than is currently the case.

2. Experimental methods

2.1. Specimens

Laser powder bed fusion was used to manufacture 316L stainless steel samples with dimensions of 10 mm x 10 mm x 15 mm. The feedstock powder had a nominal composition shown in Table 1 and an average diameter of 50 μm. Printing was conducted in an EOS M 290 machine under an argon atmosphere at a pressure 0.7 bar. A layer thickness of 40 μm was used, with a laser power of 200 W – 250 W and a laser speed of 900 mm/s – 1000 mm/s. Further details on the printing parameters used to can be found in Ref. [31].

To investigate the impact of microstructure on the response to ion irradiation, two different heat treatments were applied. The first sample was solution annealed at 1150 °C for 90 minutes and then water-quenched (WQ). The second heat treatment was applied at 1066 °C for 75 minutes and was followed by slow cooling (SC) (10 °C/minute) in an argon atmosphere. As stated in Ref. [31], these temperatures were selected such that only austenite and the $MnCr_2O_4$ spinel would be present. These two heat treatments resulted in recrystallised microstructures but there were some microstructural differences in the alloys [31]. The main difference was that there was more morphological texture in the SC 1066 °C HT sample than in the WQ 1150 °C HT sample, with melt pools still present (Supplementary Figure 1). Less recrystallisation had also occurred in the SC 1066 °C HT sample. These differences in microstructure may impact irradiation response due to a difference in the density of features, such as grain boundaries, that can act as sinks for defects such as vacancies.

The specimens were prepared for ion irradiation by first sectioning in the plane perpendicular to the build direction (Fig. 1(a)). Sections of width 0.5 mm were ground and then polished using diamond suspension to a surface finish of 0.1 μm. The polished surfaces, which represented the plane perpendicular to the sample build direction, were then exposed to ion irradiation (Fig. 1(b)).

2.2. Ion irradiations

Ion irradiations were performed at the JANNuS irradiation facility in Orsay, France. 5 MeV Ni^{2+} ions were used to irradiate both the SC 1066 °C HT and WQ 1150 °C HT samples, with the temperatures, fluxes, and fluences for individual irradiations shown in Table 2. The ion irradiation conditions were chosen to enable direct comparison with previous work on wrought 316L alloys that were characterised after ion irradiation [16].

Damage calculations as a function of depth from the irradiated surface were estimated using Stopping and Range of Ions in Matter (SRIM - v. SRIM-2013.00) software and the formulae proposed in Ref. [32]; a composition of pure Fe was used alongside the Kinchin-Pease

Table 1
Nominal composition (wt. %) of 316L powder used as feedstock to manufacture samples.

Element	Fe	Cr	Ni	Mo	Mn	Si	Cu	N	C	P
Wt. %	63.39–64.77	17.12–17.72	13.30–14.03	2.64–2.82	1.55–1.68	0.35	0.03–0.04	0.07–0.08	0.02	0.009–0.013

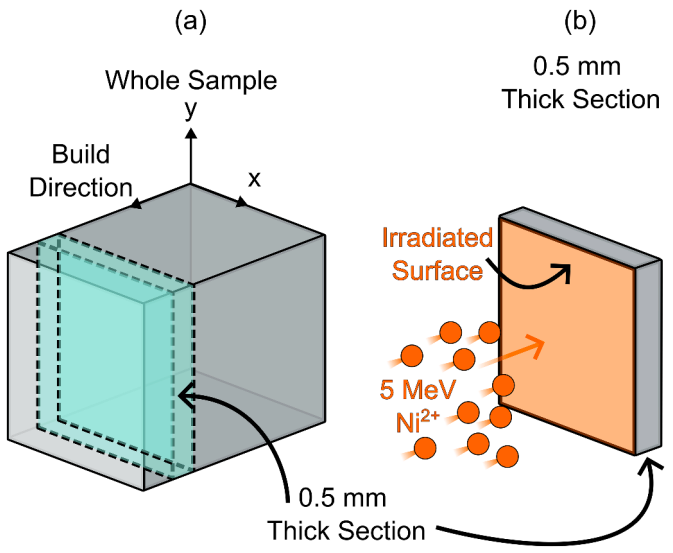

Fig. 1. Schematic indicating the orientation relationship between (a) the sample build direction and the plane sectioned for analysis and (b) the sample build direction and the direction of incident ions from the ion irradiation.

Table 2
Ion irradiation conditions used for samples in this study (5 MeV Ni^{2+} ions).

Irradiation Condition	Temperature (°C)	Fluence (ions/cm^2)	Flux (ions/cm^{2}s)	Calculated Damage at 500 nm (dpa)
Low Fluence, Low Temperature	200	2×10^{15}	2.85×10^{11}	0.75
High Fluence, Low Temperature	200	1×10^{16}	6.1×10^{11}	3.75
Low Fluence, High Temperature	450	2×10^{15}	2.85×10^{11}	0.75
High Fluence, High Temperature	450	1×10^{16}	5.2×10^{11}	3.75

approximation and a displacement threshold energy of 40 eV, as suggested in Ref. [32]. Fig. 2 shows the damage profiles for the high and low fluence samples. The Bragg peak is at a depth of around 1600 nm, whilst the dpa (displacements per atom) at target depths of 400 nm – 600 nm is determined to be 3.75 dpa and 0.75 dpa for the high and low fluence samples, respectively.

2.3. Atom probe tomography

Samples were prepared for atom probe tomography (APT) analysis using a Gallium Helios 5 UX dual beam SEM-FIB. Standard procedures, currents, and accelerating voltages were used for sample milling [33,34]. A final polishing stage using 2 keV Ga^+ ions was applied in order to ensure that the apex of the tip was 400 nm below the irradiated specimen surface; the low keV polish also had the advantage of minimising Ga implantation and associated damage [35]. Multiple APT lift-outs were taken from each specimen at different locations in an attempt to mitigate against sampling biases.

APT experiments were conducted using a LEAP 5000 XR in the GENESIS facility at the Université de Rouen Normandie. Data were collected in voltage-pulsing mode using a pulse fraction of 20 %, a detection rate of 0.003 ions per pulse, a pulse frequency of 200 kHz, and a specimen temperature of 50 K.

The APT data were reconstructed using Cameca's integrated

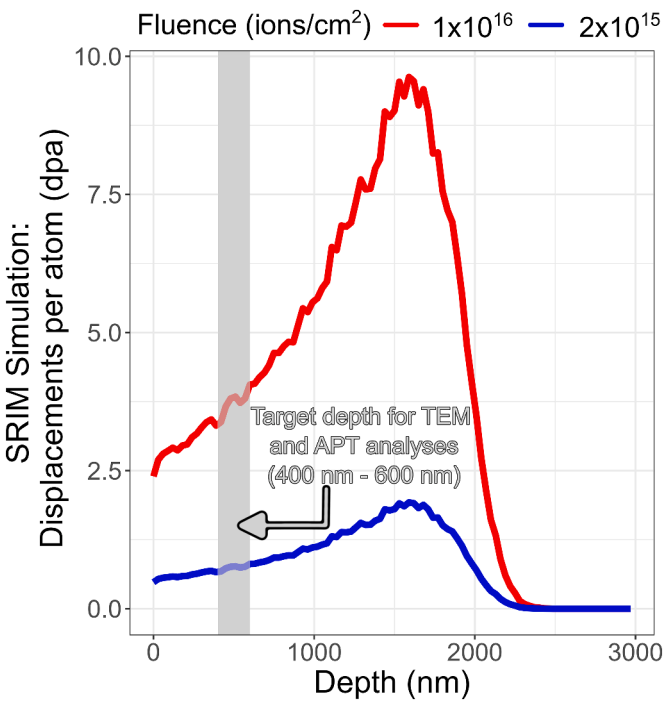

Fig. 2. Damage profile as a function as depth calculated using SRIM for 5 MeV Ni^{2+}. The depth targeted for TEM and APT analyses is highlighted (400 nm – 600 nm).

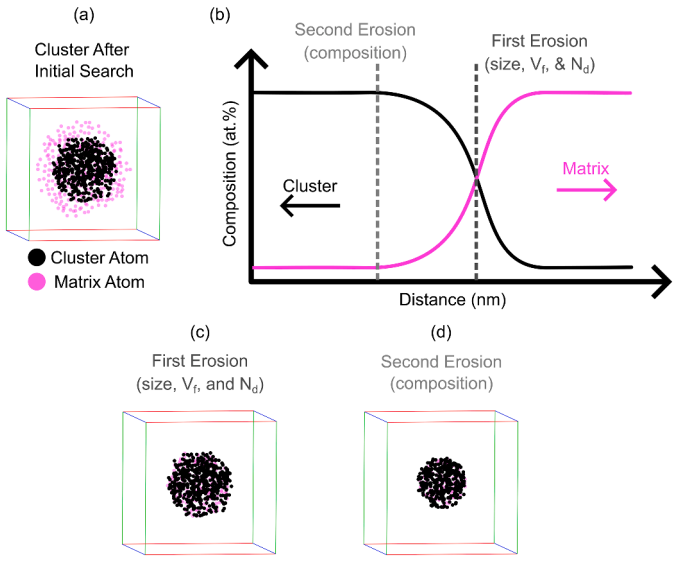

Fig. 3. Schematic diagram indicating how the erosion distances were determined and the effect that this can have on an individual cluster. Size, V_f, and N_d calculations were performed after the first erosion step whilst compositional calculations were performed after the second erosion.

visualisation and analysis software (IVAS) v3.8.16 [36,37]. Further analyses, including image generation and cluster analyses, were performed using GPM 3DSAT software (CNRS IDDN: IDDN. FR.001.430017.000.S.P.2020.000.10000). The Iso-Position method, as described in Refs. [38–40], was used to identify clusters. Since the nature of the clustering was different in each irradiation condition, the exact parameters (including the clustering elements) employed changed from dataset to dataset and are provided in Supplementary Material File 1. However, the methodology applied was consistent and consisted of:

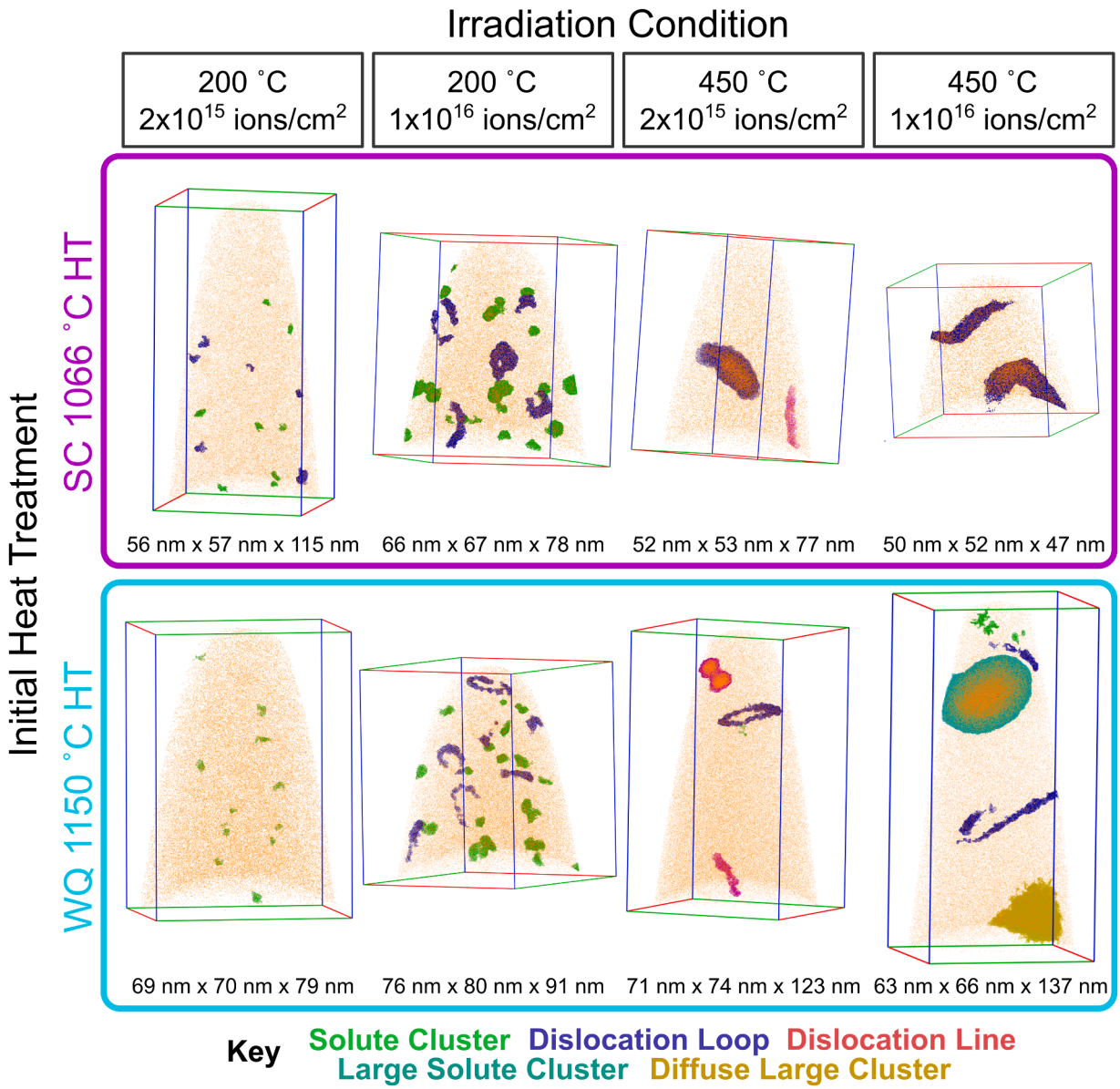

Fig. 4. Atom maps for the SC 1066 °C and WQ 1150 °C samples that were subsequently irradiated with 5 MeV Ni^{2+} ions. Key microstructural features that form after irradiation and were identified using the Iso-Position cluster search method are shown; these include Solute Clusters, Dislocation Loops, Dislocation Lines, Large Solute Clusters and Diffuse Large Clusters. The dimensions of each APT reconstruction are provided and the images were captured before erosion steps were applied to the identified clusters.

1) The threshold concentration cut-off value for atom filtering was calculated using a species expected to be clustered (in the following example, Si). This calculation was performed by dividing the dataset into 1 nm x 1 nm x 1 nm voxels and determining the Si concentration in each voxel before assigning a local Si composition to each atomic position using delocalisation with a value of 0.5 nm. The experimentally-observed frequency distribution of the Si concentrations of each atomic position was compared to that observed in a mass-randomised dataset and threshold values were selected such that each filtered atomic position contained a Si concentration that would only be expected in <0.01 % of cases in an equivalent mass-randomised dataset. Typical values were in the range of 2.5 to 4.4 at. % Si for different irradiation conditions.
2) The atomic positions that exceeded the threshold concentration of Si were filtered and cluster searches were applied solely to these atoms.
3) Cluster searches were performed with a link distance of 0.4 nm whilst the minimum number of solute atoms (as defined in Step 1) required to constitute a cluster were determined by plotting N_{min} against the number of identified clusters. Values in the plateau region were selected, with N_{min} varying between 10 and 30 solute atoms in different datasets.
4) Clusters were assigned to different families based on their morphology. These families were 'Solute Cluster', 'Dislocation Loop', 'Dislocation Line', 'Large Solute Cluster', 'Diffuse Large Cluster', and 'Grain Boundary/Other'. 'Large Solute Cluster' features were differentiated from 'Diffuse Large Cluster' features based on their morphology, with 'Diffuse Large Cluster' features exhibiting a rugged interface with the matrix.
5) Erosion steps were performed to remove matrix atoms from the edges of the clusters, and this is shown schematically in Fig. 3. The erosion steps were implemented by assigning clusters from each morphology family into size classes of 1000 atoms. For each of these cluster subsets, composition profiles were plotted against distance from the cluster-matrix interface (Fig. 3(b)). From these profiles, first erosion

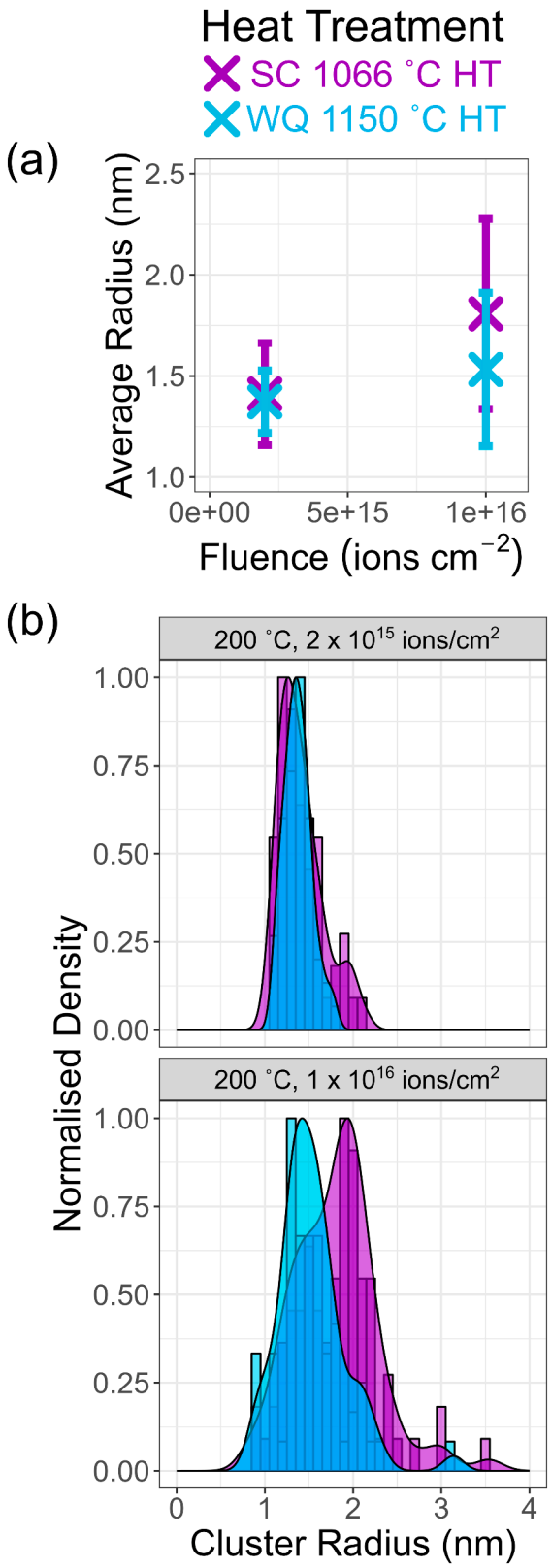

Fig. 5. Evolution of solute cluster size with irradiation dose for the samples irradiated at 200 °C. (a) shows the change in mean cluster size with ion fluence and (b) shows how the cluster size distribution compares between the two initial heat treatments and how it evolves with irradiation dose. N.B. that the density is normalised to 1 for each irradiation condition and initial heat treatment.

cut-offs were determined as the midpoint between the compositional plateaus in the cluster and the matrix. Second erosion cut-offs were set such that only the plateau region within the cluster core were chosen. The effect that each of these erosion steps can have on an individual cluster are visible in Fig. 3(c) and (d).

6) Cluster number densities, volume fractions, and sizes were calculated after the first erosion step, and compositional calculations were performed after the second erosion step. Edge clusters were not included in size calculations and were counted as half for N_d calculations. Edge clusters were not included in compositional calculations unless specified in the text.

Complete details on the cluster search parameters applied to each dataset are provided in Supplementary Material File 1.

2.4. Transmission electron microscopy

Transmission electron microscopy (TEM) lamellae were prepared with a Gallium Helios 5 UX dual beam SEM-FIB [41]. Final back-thinning of the lamellae to between 80 nm and 100 nm thickness was carried out using 0.5 keV Ar^+ ions with a Gatan Precision Ion Polishing System II (PIPS II) [42]. TEM images were centred at a depth of 400 nm – 600 nm in order to target the desired dpa zone indicated by the SRIM profile in Fig. 2. In the majority of cases, TEM was performed on a double-corrected JEOL-ARM200CF microscope at the Université de Rouen Normandie, equipped with a cold field emission gun (FEG) and operating at 200 kV. The TEM data on the samples irradiated at 450 °C to 2 × 10^{15} ions/cm^2 was obtained with a JEOL JEM-2100 at the University of Oxford's Department of Materials. This instrument had a LaB_6 electron source and was operated at 200 kV.

Imaging of the irradiation damaged regions was performed in both TEM and scanning TEM (STEM) modes. Unless indicated otherwise, images were collected in the ⟨110⟩ zone axis, $\boldsymbol{g} = 200$ two beam condition, since all visible edge-on dislocations in FCC materials in this condition can be assumed to be faulted (Frank) loops [43]. Xiu et al. also show that, in this imaging condition, four out of the six Perfect Loop families will be visible, but that none of these visible loops will be edge-on [43]. Where indicated below, STEM mode was used to reduce bend contour contrast [44], with the 3 g spot selected for low angle annular dark field images. Sample thicknesses in the analysed regions were estimated from energy-filtering transmission electron microscope (EFTEM) images. Post processing of images was carried out using DigitalMicrograph v3.42.3048.0 and ImageJ v1.54g.

Whilst there are several limitations associated with accurately quantifying dislocation loop densities via TEM, it does enable qualitative comparison between similar samples that have been exposed to different irradiation conditions. Factors which can impact the accuracy of dislocation loop quantification include: the annihilation of dislocations at free surfaces as the sample undergoes final thinning [45]; identification of small loops/black dots [46]; inter-operator variability [47]; and dislocation loop size and number density variability between variants of dislocation type [16]. In order to account for potential discrepancies between different operators, dislocation loop identification was carried out independently by two separate researchers on each micrograph. A size threshold of 3 nm was used to differentiate between dislocation loops and black dots. Dislocation loops that intersected the edge of micrographs or regions or interest were counted as 0.5 for N_d calculations and were not included in size distributions. Edge-on Frank loops were identified based on the orientation relationship between their major axis and **g**, and the ratio of the length of the major and minor axis.

Where presented in the text, number density and diameter calculations for Frank Loops are based solely upon edge-on dislocation loops in the micrographs as these are the only visible dislocations that one can be certain are not Perfect Loops in the imaging condition used. Total dislocation loop densities refer only to visible dislocation loops greater than 3 nm in diameter and do not account for the two Perfect Loop

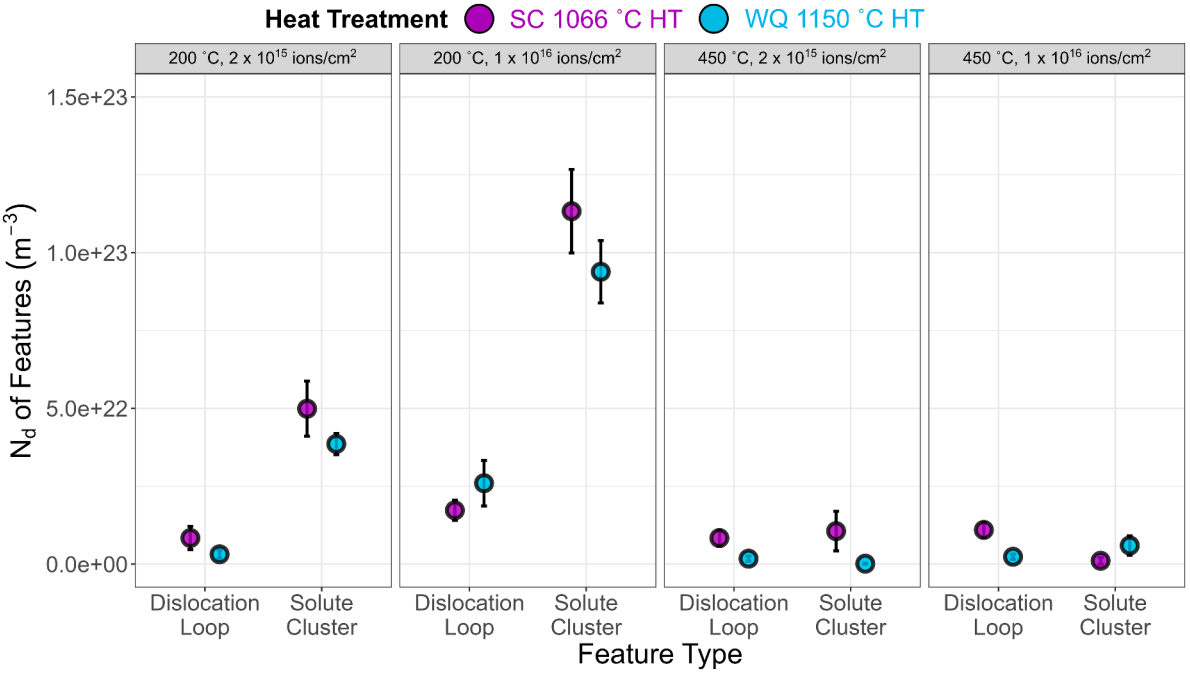

Fig. 6. Graphs showing variation in the number density of solute clusters and dislocation loops as a function of irradiation condition, as measured by APT.

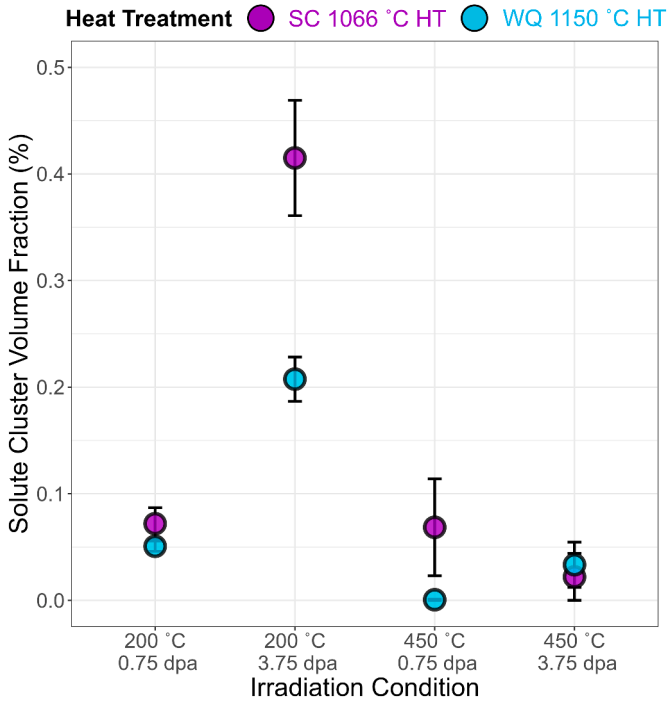

Fig. 7. Graph showing how solute cluster volume fraction varies as a function of initial heat treatment and irradiation condition, as measured by APT.

families ($\frac{a}{2}$ [011] and $\frac{a}{2}$ [01$\bar{1}$]) that are invisible in the ⟨110⟩ zone axis, $\boldsymbol{g}$ = 200 condition.

2.5. Nanoindentation

Nanoindentation was performed at the University of Oxford using a Bruker Hysitron TI Premier Nanoindenter with a diamond Berkovich tip and a MiltiRange dynamic NanoProbe™. Prior to testing, the indenter tip geometry was calibrated using a standard calibration routine, into a reference material of fused silica [48].

Data were obtained using two different experimental approaches. Firstly, quasi-static indentation, with a maximum load of 10 mN and loading rate of 2 mN/*sec*, was used to determine the modulus and hardness of each specimen. Twenty-five indents were performed on each specimen using a 5 × 5 array with a spacing of 25 μm between each indent to ensure that there was no interaction between plastic zones. Secondly, a continuous stiffness measurement (CSM) was performed to assess the variation in hardness across the non-uniform damage profile (Fig. 2), from which a dynamic measurement of hardness and modulus as a function of indentation depth was obtained. Similar to the quasi-static tests, a 5 × 5 array with 25 μm spacing between each indent was used for each sample. Dynamic measurements were made to a maximum load of 10 mN which achieved a maximum displacement of approximately 1300 nm over a 30 s loading interval. Data for both test types were analysed using Triboscan software and plotted using R v.4.2.1.

3. Results

3.1. Atom probe tomography

Multiple APT datasets were obtained for each heat-treated alloy in each irradiation condition. Fig. 4 shows that small solute clusters form after irradiation to 2 × 10^{15} ions/cm^2 at 200 °C, alongside features that may be very small dislocation loops. As the fluence increases to 1 × 10^{16} ions/cm^2 an increase in the number density, volume fraction, and size of both solute clusters and dislocation loops in the samples irradiated at 200 °C is visually-apparent.

Fig. 5(a) shows the mean measured solute cluster radius increases with dose in the samples irradiated at 200 °C. The variance within the cluster size distributions also increases with dose; histograms of cluster size in Fig. 5(b) confirm that this is the case, with an increased number of large clusters present after irradiation to 1 × 10^{16} ions/cm^2. Although both heat-treated alloys demonstrate an increased fraction of large clusters, this increase does appear more pronounced in the SC 1066 °C HT samples. Fig. 6 shows that the number density of clusters in the SC 1066 °C HT and WQ 1150 °C HT samples irradiated at 200 °C increases by a factor of around 2 between the low and high fluence conditions.

Table 3
Composition of clusters and dislocations that form after 5 MeV Ni^{++} irradiation, as measured by APT. N.B. Due to the large sizes of the dislocation loops observed at 450 °C, all dislocation loops intersected the edge of the analysed volume and so were included in the compositional calculations for these irradiation conditions.

Heat Treatment	T_{irr} (°C)	Fluence (ions/cm^2)	Feature Type	APT-Measured Composition (at. %)							
				Fe	Ni	Cr	Si	Mn	Mo	P	Other
SC 1066 °C HT	200	2×10^{15}	Cluster	56.6 ± 10.3	18.8 ± 7.5	12.9 ± 7.1	8.9 ± 6.6	0.9 ± 0.8	1.1 ± 1.6	0.3 ± 0.4	0.5 ± 0.7
			Dislocation Loop	56.3 ± 2.8	18.9 ± 3.3	15.2 ± 3.7	7.3 ± 1.4	0.8 ± 0.5	1.2 ± 0.8	0.0 ± 0.0	0.3 ± 0.3
		1×10^{16}	Cluster	49.5 ± 7.4	24.8 ± 6.5	11.4 ± 4.1	10.8 ± 3.4	0.9 ± 1.2	1.4 ± 2.8	0.5 ± 0.6	0.7 ± 0.6
			Dislocation Loop	53.8 ± 2.5	23.2 ± 2.3	12.3 ± 1.3	8.4 ± 1.4	0.8 ± 0.3	0.6 ± 0.2	0.3 ± 0.3	0.5 ± 0.2
	450	2×10^{15}	Dislocation Loop	47.4 ± 4.4	31.7 ± 5.5	10.3 ± 2.2	8.2 ± 0.3	0.4 ± 0.2	0.5 ± 0.2	1.0 ± 0.8	0.5 ± 0.1
		1×10^{16}	Dislocation Loop	45.4 ± 4.3	36.1 ± 4.9	8.6 ± 2.0	7.6 ± 2.0	0.3 ± 0.2	0.6 ± 0.3	0.6 ± 0.7	0.7 ± 0.3
WQ 1150 °C HT	200	2×10^{15}	Cluster	56.2 ± 7.3	18.2 ± 5.3	14.7 ± 4.2	8.0 ± 3.4	1.3 ± 1.7	0.8 ± 1.0	0.1 ± 0.3	0.7 ± 1.2
			Dislocation Loop	58.0 ± 0.9	15.5 ± 2.7	13.7 ± 0.8	9.7 ± 2.3	1.7 ± 1.0	0.7 ± 0.3	0.2 ± 0.2	0.5 ± 0.5
		1×10^{16}	Cluster	46.5 ± 6.9	27 ± 7.2	11.4 ± 4.4	12.4 ± 3.5	0.9 ± 1.2	0.8 ± 0.9	0.6 ± 0.8	0.6 ± 0.6
			Dislocation Loop	52.8 ± 4.9	23.3 ± 3.1	12.6 ± 1.5	8.8 ± 1.6	0.7 ± 0.4	0.9 ± 0.4	0.3 ± 0.4	0.6 ± 0.4
	450	2×10^{15}	Dislocation Loop	49.9 ± 4.7	28.2 ± 3.2	11.2 ± 1.1	8.2 ± 3.4	0.4 ± 0.3	0.7 ± 0.2	0.8 ± 0.9	0.6 ± 0.1
		1×10^{16}	Dislocation Loop	49.7 ± 5.7	31.7 ± 5.1	9.9 ± 2.1	6.9 ± 2.8	0.3 ± 0.1	0.6 ± 0.2	0.4 ± 0.3	0.6 ± 0.2

Table 4
Composition of large and diffuse solute clusters formed after Ni^{++} ion irradiation at 450 °C, as measured by APT. The measurement of the composition of the large solute clusters was performed using a 5 nm x 5 x nm x 5 nm ROI placed at the centre of the cluster, whilst the compositions for the diffuse solute clusters were taken after Iso-Position cluster searches and the second erosion step.

Feature Type	Heat Treatment	Fluence (ions/cm^2)	APT-Measured Composition (at. %)							
			Fe	Ni	Cr	Si	Mn	Mo	P	Other
Large Solute Clusters	SC 1066 °C HT	1×10^{16}	7.3	60.4	5.8	18.4	0.7	1.5	5.2	0.7
	WQ 1150 °C HT	1×10^{16}	13.1	59.7	3.8	19.6	0.4	0.6	2.2	0.6
Diffuse Solute Clusters	WQ 1150 °C HT	2×10^{15}	53.5 ± 5.8	23.7 ± 8.1	11.8 ± 3.2	8.3 ± 2	0.6 ± 0.6	0.8 ± 0	0.5 ± 0.5	0.8 ± 0.4
	SC 1066 °C HT	1×10^{16}	48.1 ± 8.3	31.5 ± 7.8	10.6 ± 2.8	6.9 ± 4.3	0.6 ± 0.2	1.1 ± 0.5	0.5 ± 0.8	0.7 ± 0.3
	WQ 1150 °C HT	1×10^{16}	47.3 ± 6	31.7 ± 3.9	10.1 ± 1.7	7.3 ± 2.2	0.5 ± 0.2	0.9 ± 0.3	1.2 ± 1.4	1.1 ± 1.1

Combining this information with Fig. 5 enables one to deduce that this increase in solute cluster number density is due to the continued formation of smaller solute clusters ($r < 1.5$ nm), whilst the solute clusters that were present at low fluence likely grow into the larger features that are observed at high fluence. Fig. 6 shows that some dislocation loops were observed in the 200 °C, 2×10^{15} ions/cm^2 samples; these features had an average diameter of 6 nm and may represent small dislocation loops that are commonly referred to as "black dots" in TEM literature [18]. The main visual difference between the samples irradiated at 200 °C and 450 °C is that the observed features are much coarser in the 450 °C samples and present in lower number density. These visual observations are supported by quantitative analyses performed after cluster searches (Fig. 6).

The evolution of solute cluster volume fraction with irradiation condition is displayed in Fig. 7 for the SC 1066 °C HT and WQ 1150 °C HT samples. The highest volume fraction of solute clusters was present in the SC 1066 °C HT sample irradiated to 1×10^{16} ions/cm^2 (3.75 dpa) at 200 °C. Aside from the 200 °C, 1×10^{16} ions/cm^2 condition, the volume fraction of solute clusters did not appear to be strongly dependent on the initial heat treatment that the alloys had undergone.

The compositions, as measured by APT, of the segregation around dislocation loops that form after ion irradiation are provided in Table 3, alongside the compositions of the solute clusters that form after irradiation at 200 °C. Solute clusters and dislocation loops in all conditions were enriched in solute compared to the matrix, with Ni and Si demonstrating the greatest affinity for these features after irradiation. Some general trends are visible in Table 3, such as that the amount of Ni and Si that is present in these features increases as dose increases from 2 $\times$ 10^{15} ions/cm^2 to 1 $\times$ 10^{16} ions/cm^2. It is also apparent that the compositions of features that form in the SC 1066 °C HT and the WQ 1150 °C HT samples under the same irradiation conditions are comparable. The dislocation loops observed after irradiation at 450 °C have a higher Ni content than those formed at 200 °C.

Large dislocation loops, which often intersected the edge of the analysed volume, were frequently characterised alongside large solute clusters and diffuse large solute clusters in the samples irradiated at 450 °C. Fig. 4 shows an APT volume from the WQ 1150 °C HT sample irradiated to 1×10^{16} ions/cm^2 at 450 °C that contains both a large solute cluster and a diffuse large solute cluster. The key differences between these two feature types are that large solute clusters are dense features that are highly enriched in solute at their core whilst diffuse solute clusters do not have a clearly defined interface with the matrix and are much less enriched in solute; the composition of these features is presented in Table 4. Due to the relatively large size and low number density of the large solute clusters, only one was characterised in each heat treatment condition. In addition to the observation that the large solute clusters contain less Fe and Cr than the diffuse solute clusters, they are also significantly more enriched in P, Ni, and Si.

3.2. Transmission electron microscopy

TEM micrographs showing the evolution of irradiation damage as a

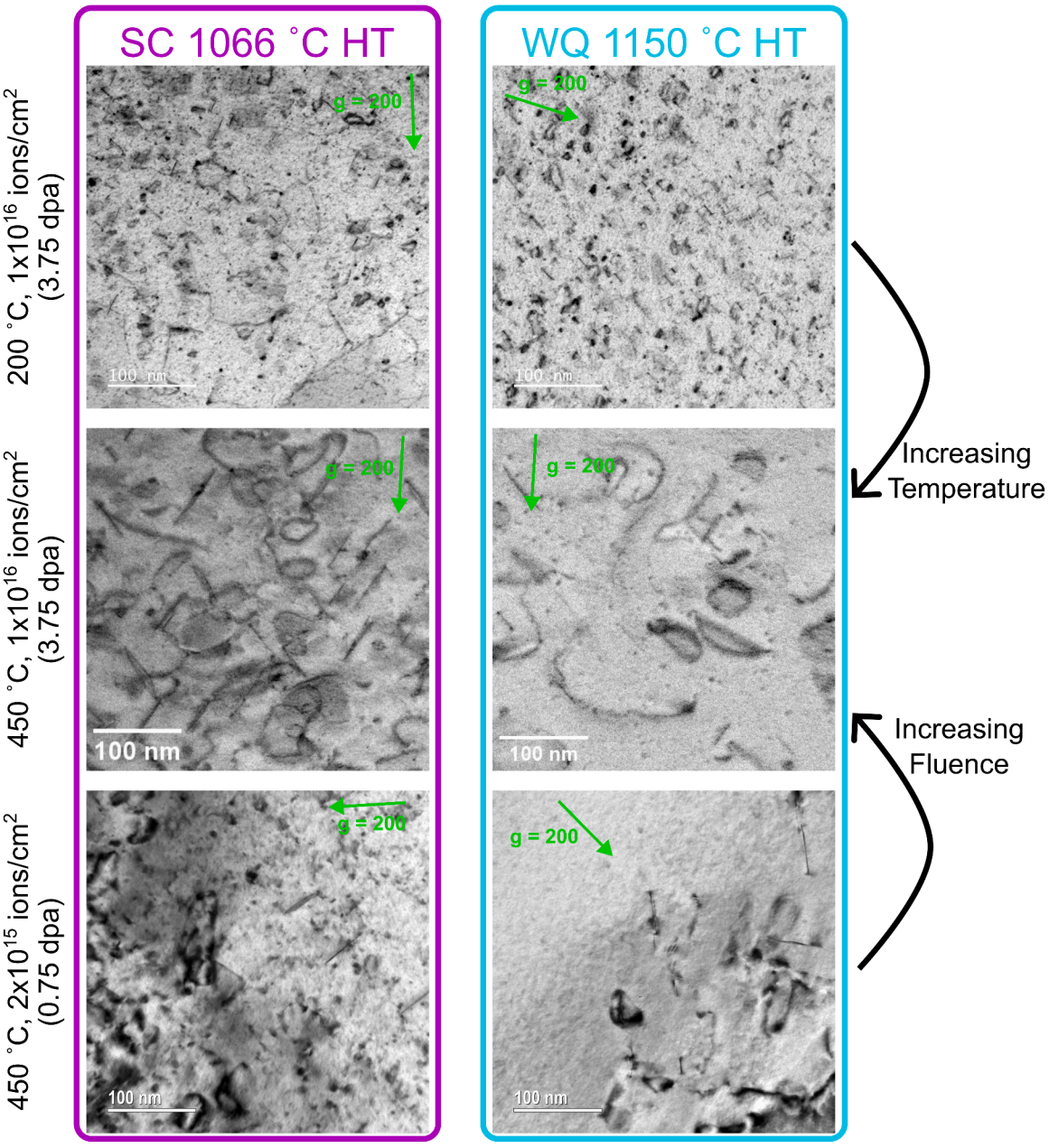

Fig. 8. TEM micrographs showing evolution of defects as a function of irradiation dose and irradiation temperature. All images were taken in the [110] zone axis, $g = 200$ condition – the 200 °C 1 × 10^{16} ions/cm^2 are STEM-HAADF images, the 450 °C 1 × 10^{16} ions/cm^2 micrographs are inverted STEM-LAADF images, the 450 °C 2 × 10^{15} ions/cm^2 micrographs were taken in bright field TEM mode. The regions used for dislocation counting quantification are shown in Supplementary Figure 3.

function of irradiation temperature and fluence, and initial sample heat treatment are shown in Fig. 8. TEM was not performed on the 200 °C 0.75 dpa samples as the APT data indicated that the features that formed in this condition would not be resolvable in the TEM. There is a clear trend for increased number density of features at higher fluences, and for coarser features to develop at elevated temperature; this is demonstrated quantitatively in Fig. 9. Whilst there are some inter-operator variations at each irradiation condition, these were far smaller than the changes measured between irradiation conditions.

Total visible dislocation loop (including Frank and Perfect) and black dot number densities are highest in the 200 °C samples irradiated to an ion fluence of 1 × 10^{16} ions/cm^2. There does not appear to be statistically significant differences between the two different heat treatments. There is a clear trend for increasing Frank Loop diameter with increasing irradiation temperature and fluence (Fig. 9(d)), with the Frank Loops having an average diameter of 35 nm in the 450 °C, 1 × 10^{16} ions/cm^2 samples compared to 8 nm in the 200 °C, 1 × 10^{16} ions/cm^2 samples. Again, the size of the features does not appear dependent upon the initial heat treatment temperature.

3.3. Nanoindentation

The nanoindentation results in Fig. 10 show that the measured hardness and modulus values of the non-irradiated samples are similar to those expected in 316L steels [49,50]. It can be seen that hardness increases as a function of both elevated irradiation dose and decreasing irradiation temperature, with the largest degree of hardening observed in the samples irradiated to 3.75 dpa at 200 °C. The same trend is present in both alloys, although the absolute values of hardness in the WQ 1150 °C HT sample are lower than those observed in the SC 1066 °C HT

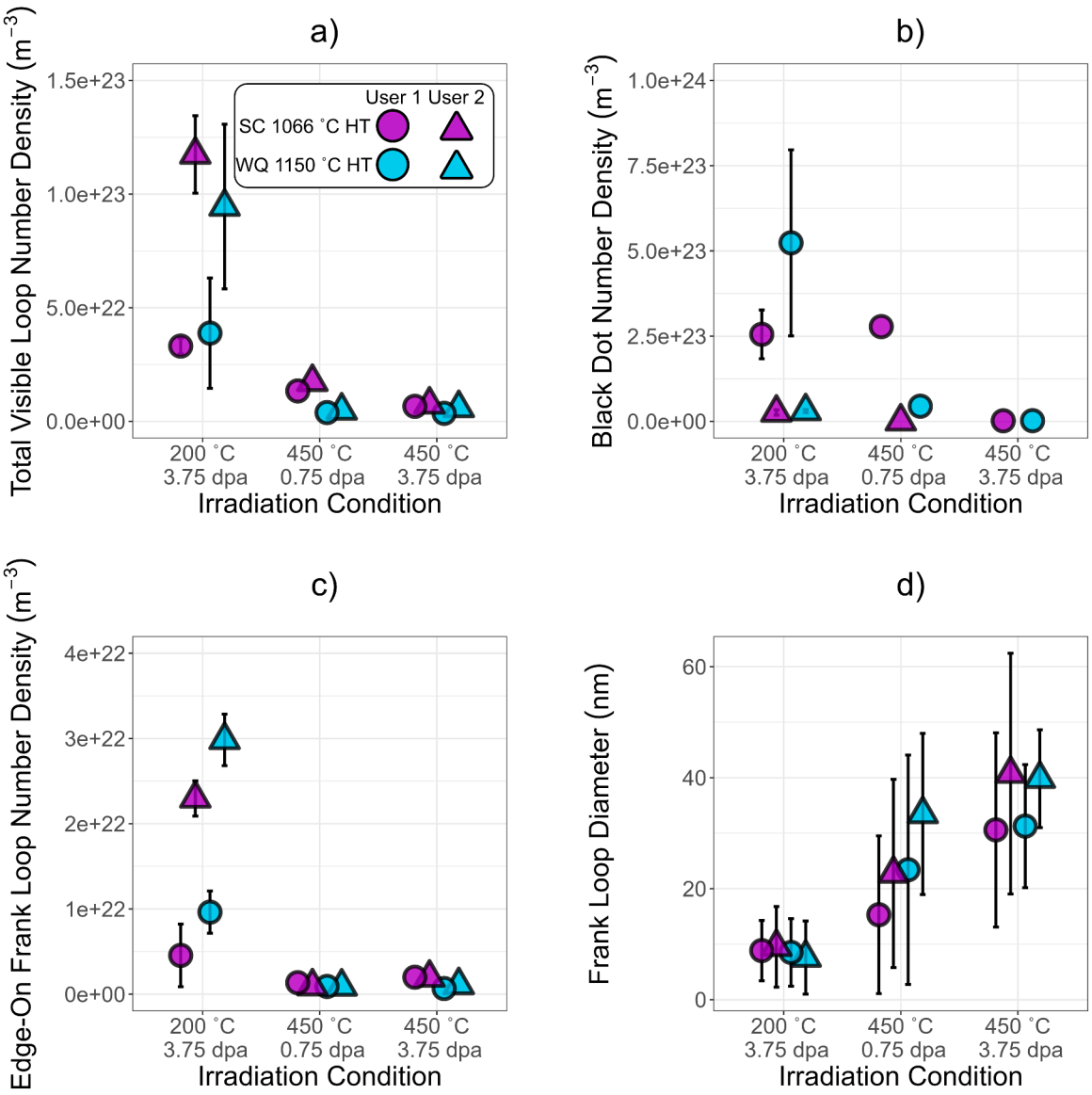

Fig. 9. Graphs showing a) Total Visible Loop Number Density, b) Black Dot Number Density, c) Frank Loop Number Density, and d) Frank Loop Diameter as a function of irradiation condition and sample heat treatment temperature.

sample in both the unirradiated and irradiated cases. Since multiple grains were sampled for each sample, these differences are unlikely to correspond to the crystallographic orientation of the grains that were sampled in the samples. Comparing nanoindentation hardness measurements between different studies, conducted using different instruments on materials irradiated with dissimilar particles and ions, is far from straightforward and subjected to multiple uncertainties. However, the hardness increases reported here are reasonably consistent to those reported on wrought 316L exposed to irradiation [50–52].

Fig. 10(b) shows a lower elastic modulus measured for the unirradiated samples compared to the irradiated samples. This property is not expected to change as a result of irradiation damage, and can be attributed to uncertainty in the measurements. The measurements from unirradiated samples, mounted with a larger amount of silver epoxy, will have measurements that contain a larger error from compliance, causing a lower apparent hardness and modulus of the material. However, the mounting method was consistent between heat treatments, and for all of the irradiation conditions in the irradiated samples. Therefore, while we cannot confidently comment on the absolute increase in hardness due to irradiation damage, we can comment on the variation between the different heat treatments and the variation between different irradiation conditions.

The results from the CSM tests on the non-irradiated and irradiated alloys are presented in Fig. 11, whilst the change in hardness compared to the non-irradiated condition for each alloy is shown in Fig. 12. There is a clear trend for increasing hardness with increased irradiation dose, with a larger degree of hardness change measured at lower irradiation temperatures. There was no appreciable difference between the hardness change observed in the SC 1066 °C HT and WQ 1150 °C HT samples.

Indentation size effects convolute irradiation hardness measurements at shallow depth, making it difficult to explicitly measure irradiation induced hardening of shallow ion-irradiated layers. Previous work has demonstrated that by applying the Nix and Gao model, measurements of hardness that are independent of size, may be obtained [52–54]. From the CSM data in Fig. 11, h^2 vs 1/h was plotted; these plots showed a bilinear trend with an intersection at an indentation depth of approximately 330 nm. This transition indicates that the plastic zone had extended to a depth beyond the ion-irradiated layer and was sampling the unirradiated material. As the Bragg peak lies approximately

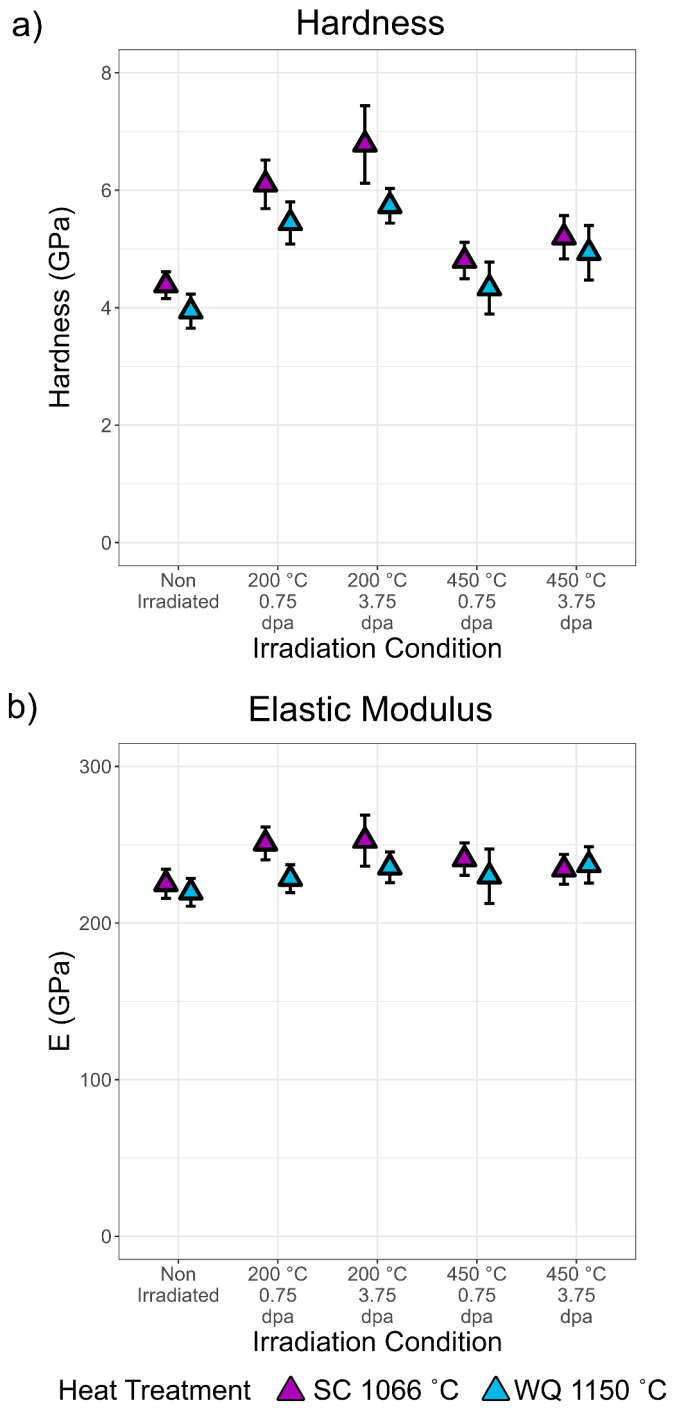

Fig. 10. Nanoindentation results showing how the (a) hardness and (b) elastic modulus varies as a function of irradiation condition for the samples heat-treated at 1066 °C and 1150 °C.

2000 nm below the surface (Fig. 2), this would give an estimated plastic zone size of approximately six times the indentation depth, which is appropriate for metallic materials [55].

H_0 values were determined by fitting lines to the linear regions in the h^2 vs 1/h plots and calculating the intercept with the y-axis when $x = 0$ [52,53]. The H_0 values for each irradiation condition are shown in Fig. 13. The trends in Fig. 13 are consistent with those from the quasi-static testing in Fig. 10(a). The differences in the absolute values of hardness may be explained by differences in the strain rate of the two testing methods [56].

4. Discussion

There are certain trends in the data across the APT, TEM, and nanoindentation results. Firstly, that the number density of irradiation-induced features and increases in measured hardness are correlated with increasing dose and decreasing irradiation temperature. At higher irradiation temperatures, there are a lower number density of coarser features than are observed in the irradiations conducted at 200 °C.

The SC 1066 °C HT and the WQ 1150 °C HT samples appear to respond reasonably similarly to ion irradiation under equivalent irradiation doses and temperatures. However, there are some subtle differences. For example, the SC 1066 °C HT samples had a slightly higher hardness increase than the WQ 1150 °C HT counterparts after irradiation to 3.75 dpa at 200 °C (Fig. 10). Whilst the SC 1066 °C HT samples displayed slightly higher initial hardness, possibly due to the samples having a finer-grained microstructure than the WQ 1150 °C HT specimens (Supplementary Figure 1), this does not appear to fully account for the differences observed after irradiation to 3.75 dpa at 200 °C. The APT data show that the SC 1066 °C HT samples had a higher volume fraction of solute clusters in this irradiation condition, and that this was a result of the average size of the features being larger than in the WQ 1150 °C HT volumes (Fig. 5 and Fig. 7). Since solute clusters in steels are known to impede dislocation motion with increasing magnitude proportional to the square root of cluster volume fraction [57], the APT observations made here can rationalise the change in measured hardness after 3.75 dpa of damage at 200 °C. However, a model that accurately predicts hardness changes based on microstructural evolution must take a holistic approach and consider a range of other factors that can impede dislocation motion, such as the number density and sizes of features including vacancy clusters, dislocation loops that are too small to be resolved by TEM and, where present, helium bubbles.

Other than the differences discussed in the previous paragraph, it appears that the SC 1066 °C HT and WQ 1150 °C HT samples respond very similarly to one another when subjected to ion irradiation. For example, dislocation loop number densities and sizes, and cluster number densities and sizes are fairly consistent at each irradiation condition. The composition of the solute clusters and the segregation around loops measured by APT show no major differences between the two heat treatments (Table 3), indicating that similar mechanisms are operating in both sample sets. The observed solute cluster compositions in both AM alloys are very similar to those previously reported in wrought alloys [16], indicating that the proposed mechanism of solute cluster formation in wrought alloys [15,22,23] is likely also responsible for solute cluster formation in LBPF 316L. This finding is promising and demonstrates that LBPF 316L may be adopted for use in irradiation-facing environments in which wrought 316L is already used.

The observation that the SC 1066 °C HT sample had a larger volume fraction of solute clusters than the WQ 1150 °C HT sample in the 3.75 dpa, 200 °C condition is difficult to rationalise. However, since these measurements are consistent across APT samples from different regions of the irradiated surface, this observation is not likely due to sampling biases in the APT experiments. This is supported by the quasistatic and CSM nanoindentation data which is likely to have sampled multiple grains and shows that the SC 1066 °C HT had a higher hardness after irradiation to 3.75 dpa at 200 °C than the WQ 1150 °C HT sample.

Due to the segregation of solute atoms to dislocation loops at all irradiation conditions, dislocation loops were identified in the APT datasets for all irradiation conditions. Ni, Si, and P were observed to strongly segregate to the dislocations, with more Ni enrichment observed at higher irradiation temperatures. It is noteworthy that the elements which segregate to the dislocations in irradiated samples is different to those typically observed to segregate to cell walls in the as-printed materials (Cr, Mn, Mo) [31,58–60]. This may be due to Ni and Cr segregating by the inverse Kirkendall vacancy mechanism [22] and/or solute dragging by point defects in the irradiated alloys, whilst the segregation in the as-printed materials is due to solidification and

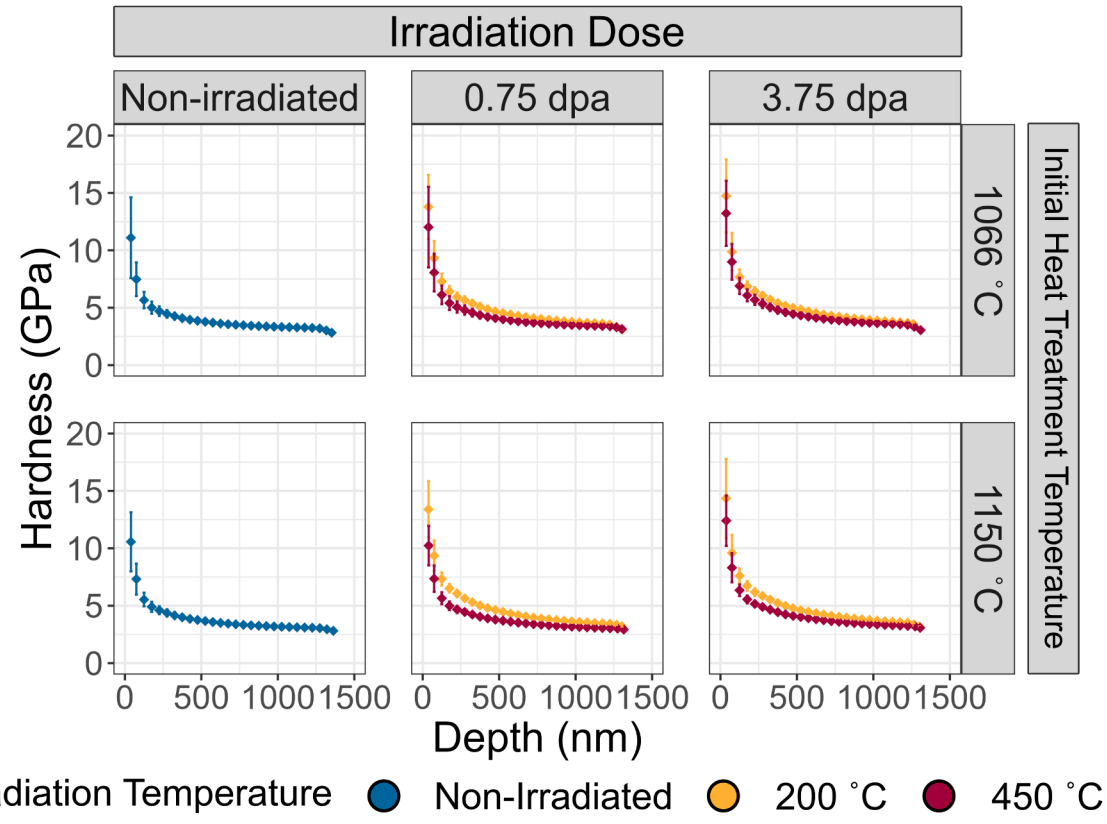

Fig. 11. CSM results showing how the hardness varies as a function of depth and irradiation condition (dose and temperature) for the samples heat-treated at 1066 °C and 1150 °C.

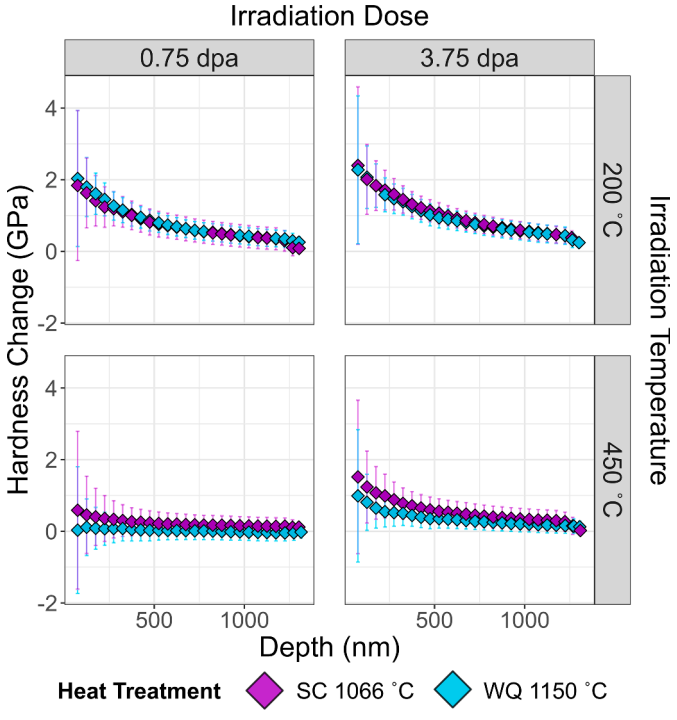

Fig. 12. CSM results showing hardness change from the non-irradiated condition as a function of depth and irradiation condition (dose and temperature) for the samples heat-treated at 1066 °C and 1150 °C.

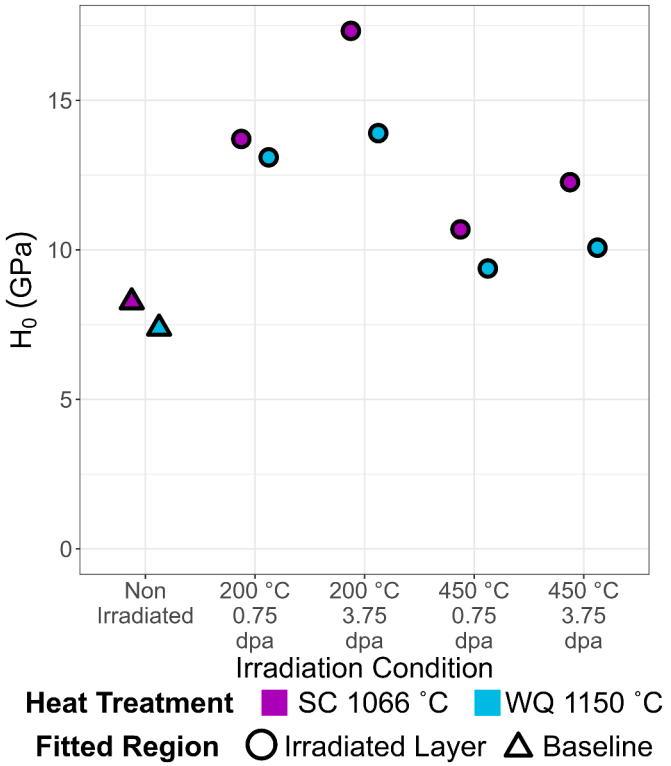

Fig. 13. H_0 values calculated by applying the Nix and Gao model to the CSM data for non-irradiated baseline material and for the ion-irradiated layer in the irradiated materials.

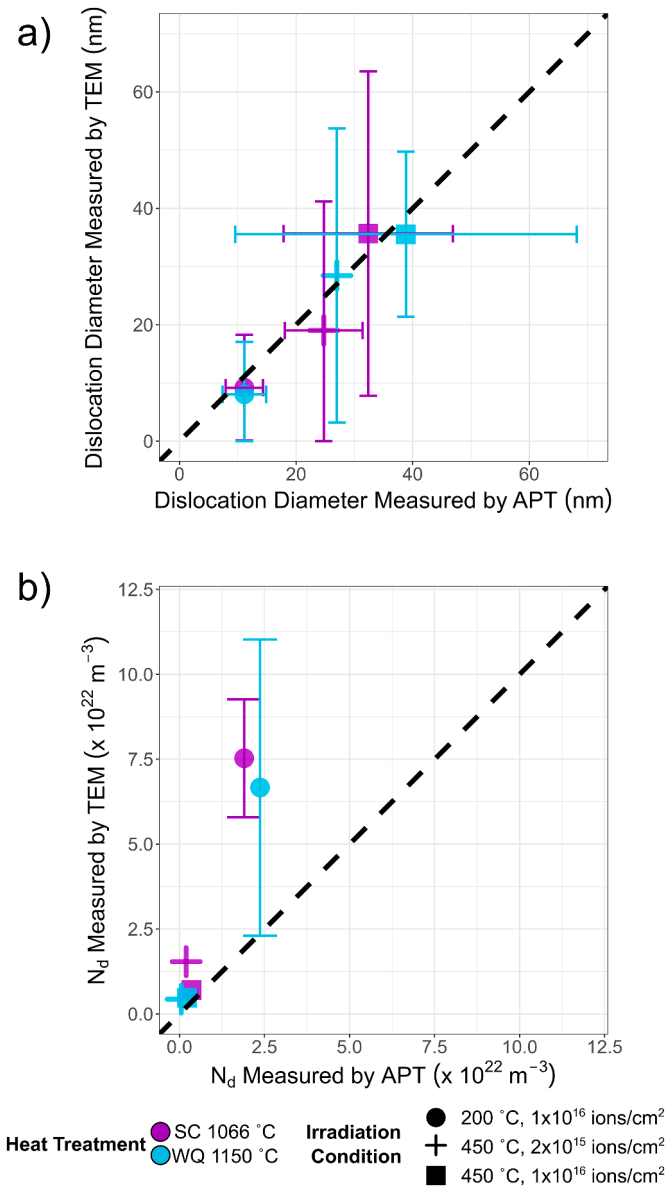

Fig. 14. Graphs showing variation between (a) the dislocation loop diameter and (b) number density of dislocations as measured by APT and TEM.

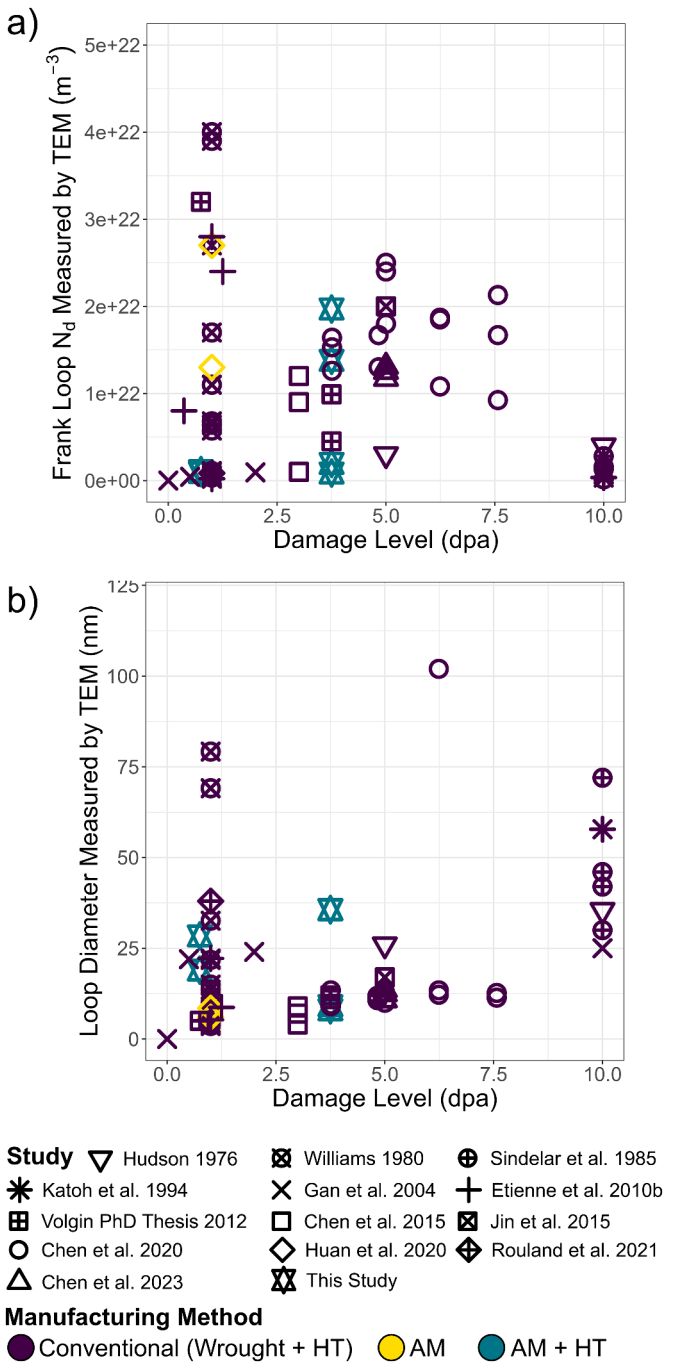

Fig. 15. Comparison between (a) dislocation densities and (b) dislocation loop diameters measured in this study to those previously reported in the literature for various Ni^{x+} or Fe^{y+} ion irradiations. Data taken from [11–17,20,22,63–67].

lethargic diffusion kinetics of the species found at the dendrite cell walls [59].

It was also possible to use APT to characterise the sizes and number densities of the dislocation loops and to compare the results to those obtained via TEM. Fig. 14a) demonstrates that the dislocation diameters measured by APT and TEM are comparable in each irradiation condition and there are no major discrepancies, thus highlighting APT's potential to accurately characterise dislocation loop sizes provided that there is strong enough solute segregation to distinguish the dislocations from the matrix. It should be noted that it was not possible to differentiate between Perfect and Frank loops in the APT data and so both are included in the dislocation diameter measurements; the good correlation between the TEM and APT-measured sizes may be indicative of Perfect and Frank loops having similar sizes in these specimens. However, Fig. 14(b) shows that the number density of dislocation loops is undermeasured by APT when compared to TEM. This undermeasurement is not entirely surprising, since APT will only be able to identify dislocations that are sufficiently enriched in solute, which may not be the case for all dislocations in the material.

As discussed during Section 2.4 Transmission Electron Microscopy, quantification of dislocation sizes and number densities in TEM can be affected by several phenomena. Our results in Fig. 9 demonstrate that although some variation is due to inter-operator variations, these differences are negligible compared to the population variance when measuring dislocation diameters. However, there are larger differences between users when quantifying dislocation number densities, although these are often less than an order of magnitude, except for when characterising black dots. This discrepancy when characterising the smallest features in the TEM micrographs is probably due to a combination of factors including variations in how operators perform background subtractions and differences in what operators believe is contrast caused by

dislocations. This is in agreement with previous work that has shown the difficulty that TEM has when determining the number density of small irradiation-induced features when compared to those predicted by simulations or measured using X-ray techniques [46,61,62].

One of the main purposes of this study was to determine if heat-treated additively manufactured 316L alloys behave similarly to wrought 316L when exposed to irradiation. Fig. 15 shows how the TEM results from this study compare to previous literature on ion-irradiated wrought 316L and AM 316L with and without post-printing heat treatment; it should be noted that the values plotted in Fig. 15 only consider irradiations conducted with Fe or Ni ions up to a maximum damage level of 10 dpa. The Frank loop number densities measured in this study are comparable to those previously reported, especially when one considers the array of variables that change between studies (e.g. irradiation temperature, dose rate, ion energy, etc.). The only appreciable difference in this study is that the size of the Frank loops measured in the samples irradiation at 450 °C to 1×10^{16} ions/cm^2 were approximately twice as large as those previously observed in wrought alloys that were irradiated under similar conditions [16]. This discrepancy may be because some of the irradiations by Volgin were conducted on thin TEM foils and not on bulk samples, which is something that the author acknowledged would impact their results and the ability to easily compare to bulk samples [16].

5. Conclusions

APT, TEM, and nanoindentation results have been used to show that the response of LBPF 316L alloys exposed to ion irradiation after two different post-printing heat treatments is similar to wrought 316L. There were shown to be no major differences in the irradiation response of the samples exposed to a post-printing heat treatment at 1066 °C followed by slow cooling compared to those heat treated at 1150 °C and water quenched. In addition, the TEM and APT results are consistent with previous studies that investigated the response of wrought 316L alloys to ion irradiation.

APT and TEM were used to characterise solute cluster and dislocation loop formation, revealing enrichment of Ni, Si, and P at solute clusters and dislocation loops compared to the matrix. Characterisation of dislocation loop size was shown to be comparable between APT and TEM. General trends for the presence of features with lower number density and larger size with increasing irradiation temperature were observed. Increased dose was correlated with increased number density and size of irradiation-induced features.

The results in this article demonstrate that LBPF 316L alloys subjected to heat treatment post printing respond very similarly to wrought 316L alloys when exposed to ion irradiation. These findings are a promising validation for the use of AM 316L to produce components exposed to irradiation during service. However, there are other factors that must be considered and investigated before AM 316L is deployed in-service. For example, validation is needed that helium bubble evolution in heat-treated AM 316L alloys is similar to wrought 316L, and investigations should be conducted into how microstructural differences between AM and wrought 316L alloys on the micron scale affect degradation processes such as stress corrosion cracking.

Funding sources

This project has received funding from the European Union's Horizon 2020 research and innovation programme under the Marie Skłodowska-Curie grant agreement No 101034329. Recipient of the WINNINGNormandy Program supported by the Normandy Region.

Experiments were performed on GENESIS platform instruments supported by the Région Haute-Normandie, the Métropole Rouen Normandie, the CNRS via LABEX EMC3 and the French National Research Agency as a part of the program "Investissements d'avenir" with the reference ANR-11-EQPX-0020. This work was supported by the European Regional Fund (ERDF) and the Normandy Region through GENESIS+ SATUP projects. This work was partially supported by the CNRS Federation IRMA - FR 3095.

TEM acquisitions on RIO camera have been performed thanks to CATHY project. European Union and Région Normandie have contributed to the realisation of CATHY project. CATHY is co-funded via the European Regional Development Fund.

Nanoindentation experiments were performed at the University of Oxford, on an instrument funded by the Henry Royce Institute (Grant ref EP/R010145/1).

JH acknowledges support from the UK EPSRC Fusion Grant 2022/27, EP/W006839/1.

CRediT authorship contribution statement

Benjamin M. Jenkins: Writing – original draft, Visualization, Software, Methodology, Investigation, Funding acquisition, Formal analysis, Conceptualization. **Solène Rouland:** Writing – review & editing, Visualization, Methodology, Investigation, Formal analysis. **Auriane Etienne:** Writing – review & editing, Investigation, Formal analysis. **Anna Kareer:** Writing – review & editing, Investigation, Formal analysis. **Jack Haley:** Writing – review & editing, Investigation, Formal analysis. **Cristelle Pareige:** Writing – review & editing, Funding acquisition. **Philippe Pareige:** Writing – review & editing, Funding acquisition. **Bertrand Radiguet:** Writing – review & editing, Methodology, Investigation, Funding acquisition, Formal analysis.

Declaration of competing interest

The authors declare that they have no known competing financial interests or personal relationships that could have appeared to influence the work reported in this paper.

Acknowledgements

This project has received funding from the European Union's Horizon 2020 research and innovation programme under the Marie Skłodowska-Curie grant agreement No 101034329. Recipient of the WINNINGNormandy Program supported by the Normandy Region.

Experiments were performed on GENESIS platform instruments supported by the Région Haute-Normandie, the Métropole Rouen Normandie, the CNRS via LABEX EMC3 and the French National Research Agency as a part of the program "Investissements d'avenir" with the reference ANR-11-EQPX-0020.

Nanoindentation experiments were performed at the University of Oxford, on an instrument funded by the Henry Royce Institute (Grant ref EP/R010145/1).

This work was supported by the European Regional Fund (ERDF) and the Normandy Region through GENESIS+ SATUP, and CATHY projects.

JH acknowledges support from the UK EPSRC Fusion Grant 2022/27, EP/W006839/1.

Supplementary materials

Supplementary material associated with this article can be found, in the online version, at doi:10.1016/j.jnucmat.2025.155913.

Data availability

Data will be made available on request.

References

[1] W.E. Frazier, Metal Additive Manufacturing: a review, JMEP 23 (2014) 1917–1928, https://doi.org/10.1007/s11665-014-0958-z.
[2] M.K. Thompson, G. Moroni, T. Vaneker, G. Fadel, R.I. Campbell, I. Gibson, A. Bernard, J. Schulz, P. Graf, B. Ahuja, F. Martina, Design for Additive

Manufacturing: trends, opportunities, considerations, and constraints, CIRP Annals 65 (2016) 737–760, https://doi.org/10.1016/j.cirp.2016.05.004.
[3] B.H. Jared, M.A. Aguilo, L.L. Beghini, B.L. Boyce, B.W. Clark, A. Cook, B.J. Kaehr, J. Robbins, Additive Manufacturing: toward holistic design, Scr Mater. 135 (2017) 141–147, https://doi.org/10.1016/j.scriptamat.2017.02.029.
[4] G. Liu, X. Zhang, X. Chen, Y. He, L. Cheng, M. Huo, J. Yin, F. Hao, S. Chen, P. Wang, S. Yi, L. Wan, Z. Mao, Z. Chen, X. Wang, Z. Cao, J. Lu, Additive Manufacturing of structural materials, Mater. Sci. Eng. R 145 (2021), https://doi.org/10.1016/j.mser.2020.100596.
[5] S.J. Zinkle, J.T. Busby, Structural materials for fission & fusion energy, Mater. Today 12 (2009) 12–19, https://doi.org/10.1016/S1369-7021(09)70294-9.
[6] S.J. Zinkle, G.S. Was, Materials challenges in nuclear energy, Acta Mater. 61 (2013) 735–758, https://doi.org/10.1016/j.actamat.2012.11.004.
[7] S.J. Zinkle, H. Tanigawa, B.D. Wirth, Radiation and Thermomechanical Degradation Effects in Reactor Structural Alloys, Elsevier Inc., 2019, https://doi.org/10.1016/B978-0-12-397046-6.00005-8.
[8] G.S. Was, Challenges to the use of ion irradiation for emulating reactor irradiation, J. Mater. Res. 30 (2015) 1158–1182, https://doi.org/10.1557/jmr.2015.73.
[9] K.L. Murty, I. Charit, Structural materials for Gen-IV nuclear reactors: challenges and opportunities, J. Nucl. Mater. 383 (2008) 189–195, https://doi.org/10.1016/j.jnucmat.2008.08.044.
[10] F. Dalle, M. Blat-Yrieix, S. Dubiez-Le Goff, C. Cabet, Ph. Dubuisson, Conventional austenitic steels as out-of-core materials for Generation IV nuclear reactors. Structural Materials for Generation IV Nuclear Reactors, Elsevier, 2017, pp. 595–633, https://doi.org/10.1016/B978-0-08-100906-2.00017-3.
[11] J.A. Hudson, Void formation in solution-treated aisi 316 and 321 stainless steels under 46.5 mev ni6+ irradiation, J. Nucl. Mater. 60 (1976) 89–106, https://doi.org/10.1016/0022-3115(76)90121-5.
[12] T.M. Williams, The effect of soluble carbon on void swelling and low dose dislocation structures in type 316 austenitic stainless steel irradiated with 46.5 MeV Ni6+ ions, J. Nucl. Mater. 88 (1980) 217–225, https://doi.org/10.1016/0022-3115(80)90277-9.
[13] R.L. Sindelar, G.L. Kulcinski, R.A. Dodd, Heterogeneous void formation in 14 MeV nickel-ion irradiated 316 SS, J. Nucl. Mater. 133–134 (1985) 544–548, https://doi.org/10.1016/0022-3115(85)90207-7.
[14] J. Gan, E.P. Simonen, S.M. Bruemmer, L. Fournier, B.H. Sencer, G.S. Was, The effect of oversized solute additions on the microstructure of 316SS irradiated with 5 MeV Ni++ ions or 3.2 MeV protons, J. Nucl. Mater. 325 (2004) 94–106, https://doi.org/10.1016/j.jnucmat.2003.11.002.
[15] A. Etienne, B. Radiguet, P. Pareige, Understanding silicon-rich phase precipitation under irradiation in austenitic stainless steels, J. Nucl. Mater. 406 (2010) 251–256, https://doi.org/10.1016/j.jnucmat.2010.08.045.
[16] A. Volgin, Characterization and Understanding of Ion Irradiation Effect On the Microstructure of Austenitic Stainless Steels, Université de Rouen, 2012. PhD Thesis, https://inis.iaea.org/search/search.aspx?orig_q=RN:46034919.
[17] D. Chen, K. Murakami, K. Dohi, K. Nishida, N. Soneda, Z. Li, L. Liu, N. Sekimura, Depth distribution of Frank loop defects formed in ion-irradiated stainless steel and its dependence on Si addition, Nucl. Instrum. Methods Phys. Res. Sect. B 365 (2015) 503–508, https://doi.org/10.1016/j.nimb.2015.08.029.
[18] S. Jublot-Leclerc, X. Li, L. Legras, M.-L. Lescoat, F. Fortuna, A. Gentils, Microstructure of Au-ion irradiated 316L and FeNiCr austenitic stainless steels, J. Nucl. Mater. 480 (2016) 436–446, https://doi.org/10.1016/j.jnucmat.2016.08.006.
[19] Z. Jiao, J. Michalicka, G.S. Was, Self-ion emulation of high dose neutron irradiated microstructure in stainless steels, J. Nucl. Mater. 501 (2018) 312–318, https://doi.org/10.1016/j.jnucmat.2018.01.054.
[20] D. Chen, K. Murakami, K. Dohi, K. Nishida, Z. Li, N. Sekimura, The effects of loop size on the unfaulting of Frank loops in heavy ion irradiation, J. Nucl. Mater. 529 (2020) 151942, https://doi.org/10.1016/j.jnucmat.2019.151942.
[21] A. Etienne, B. Radiguet, P. Pareige, J.-P. Massoud, C. Pokor, Tomographic atom probe characterization of the microstructure of a cold worked 316 austenitic stainless steel after neutron irradiation, J. Nucl. Mater. 382 (2008) 64–69, https://doi.org/10.1016/j.jnucmat.2008.09.015.
[22] A. Etienne, B. Radiguet, N.J. Cunningham, G.R. Odette, P. Pareige, Atomic scale investigation of radiation-induced segregation in austenitic stainless steels, J. Nucl. Mater. 406 (2010) 244–250, https://doi.org/10.1016/j.jnucmat.2010.08.043.
[23] T.R. Allen, G.S. Was, Modeling radiation-induced segregation in austenitic Fe–Cr–Ni alloys, Acta Mater. 46 (1998) 3679–3691, https://doi.org/10.1016/S1359-6454(98)00019-6.
[24] M. Song, M. Wang, X. Lou, R.B. Rebak, G.S. Was, Radiation damage and irradiation-assisted stress corrosion cracking of additively manufactured 316L stainless steels, J. Nucl. Mater. 513 (2019) 33–44, https://doi.org/10.1016/j.jnucmat.2018.10.044.
[25] Z. Shang, C. Fan, S. Xue, J. Ding, J. Li, T. Voisin, Y.M. Wang, H. Wang, X. Zhang, Response of solidification cellular structures in additively manufactured 316 stainless steel to heavy ion irradiation: an in situ study, Mater. Res. Lett. 7 (2019) 290–297, https://doi.org/10.1080/21663831.2019.1604442.
[26] B.P. Eftink, J.S. Weaver, J.A. Valdez, V. Livescu, D. Chen, Y. Wang, C. Knapp, N. A. Mara, S.A. Maloy, G.T. Gray, Proton irradiation and characterization of additively manufactured 304L stainless steels, J. Nucl. Mater. 531 (2020), https://doi.org/10.1016/j.jnucmat.2020.152007.
[27] S. Li, J. Hu, W.-Y. Chen, J. Yu, M. Li, Y. Wang, Evolution of cellular dislocation structures and defects in additively manufactured austenitic stainless steel under ion irradiation, Scr Mater. 178 (2020) 245–250, https://doi.org/10.1016/j.scriptamat.2019.11.036.
[28] J. Lin, F. Chen, X. Tang, J. Liu, S. Shen, G. Ge, Radiation-induced swelling and hardening of 316L stainless steel fabricated by selected laser melting, Vacuum 174 (2020) 109183, https://doi.org/10.1016/j.vacuum.2020.109183.
[29] C. Li, F. Chen, G. Ge, J. Lin, Z. Sun, M. Fan, P. Huang, X. Tang, Impact of sub-grain structure on radiation resistance in additively manufactured 316L stainless steels: an atomic insight into the mechanism, Appl. Surf. Sci. 606 (2022) 154926, https://doi.org/10.1016/j.apsusc.2022.154926.
[30] T.S. Byun, B.E. Garrison, M.R. McAlister, X. Chen, M.N. Gussev, T.G. Lach, A. L. Coq, K. Linton, C.B. Joslin, J.K. Carver, F.A. List, R.R. Dehoff, K.A. Terrani, Mechanical behavior of additively manufactured and wrought 316L stainless steels before and after neutron irradiation, J. Nucl. Mater. 548 (2021), https://doi.org/10.1016/j.jnucmat.2021.152849.
[31] B.M. Jenkins, A. Etienne, E. Baustert, G. Rose, C. Pareige, P. Pareige, B. Radiguet, Multiscale characterisation study on the effect of heat treatment on the microstructure of additively manufactured 316L stainless steel, Mater. Today Commun. 39 (2024) 108849, https://doi.org/10.1016/j.mtcomm.2024.108849.
[32] R.E. Stoller, M.B. Toloczko, G.S. Was, A.G. Certain, S. Dwaraknath, F.A. Garner, Erratum: (On the use of SRIM for computing radiation damage exposure (2013) 310 (75–80), (S0168583X13005053), (10.1016/j.nimb.2013.05.008)), Nucl. Instrum. Methods Phys. Res. Sect. B 459 (2019) 196–197, https://doi.org/10.1016/j.nimb.2019.08.015.
[33] D.J. Larson, D.T. Foord, A.K. Petford-Long, T.C. Anthony, I.M. Rozdilsky, A. Cerezo, G.D.W. Smith, Focused ion-beam milling for field-ion specimen preparation: preliminary investigations, Ultramicroscopy 75 (1998) 147–159, https://doi.org/10.1016/S0304-3991(98)00058-8.
[34] M.K. Miller, K.F. Russell, G.B. Thompson, Strategies for fabricating atom probe specimens with a dual beam FIB, Ultramicroscopy 102 (2005) 287–298, https://doi.org/10.1016/j.ultramic.2004.10.011.
[35] M.K. Miller, K.F. Russell, K. Thompson, R. Alvis, D.J. Larson, Review of atom probe FIB-based specimen preparation methods, Microsc. Microanal. 13 (2007) 428–436, https://doi.org/10.1017/S1431927607070845.
[36] F. Vurpillot, B. Gault, B.P. Geiser, D.J. Larson, Reconstructing atom probe data: a review, Ultramicroscopy 132 (2013) 19–30, https://doi.org/10.1016/j.ultramic.2013.03.010.
[37] D.J. Larson, B. Gault, B.P. Geiser, F. De Geuser, F. Vurpillot, Atom probe tomography spatial reconstruction: status and directions, Curr. Opin. Solid State Mater. Sci. 17 (2013) 236–247, https://doi.org/10.1016/j.cossms.2013.09.002.
[38] P.D. Styman, H. Weekes, J.M. Hyde, B. Radiguet, F. Vurpillot, G.Da Costa, C. Pareige, A. Etienne, P. Pareige, APT Characterisation of Radiation Damage in RPV Steels: Experimental and Data Processing Uncertainties, NUGENIA-PLUS, Nuclear Generation II & III Association, 2016.
[39] D. Blavette, I. Blum, F. Cuvilly, G.Da Costa, F. Danoix, J. Houard, W. Lefebvre-Ulrikson, C. Pareige, L. Rigutti, X. Sauvage, A. Vella, F. Vurpillot, Atom Probe tomography: Put Theory Into Practice, Academic Press, Amsterdam Boston Heidelberg, 2016 an imprint of Elsevier.
[40] A. Zakirov, Influence of the Bulk Chemical Composition on the Microstructure Evolution of Irradiated Chemically-Tailored Nuclear RPV Steels, Université de Rouen, 2022.
[41] L.A. Giannuzzi, J.L. Drown, S.R. Brown, R.B. Irwin, F.A. Stevie, Applications of the FIB lift-out technique for TEM specimen preparation, Microsc. Res. Tech. 41 (1998) 285–290, https://doi.org/10.1002/(SICI)1097-0029(19980515)41:4<285::AID-JEMT1>3.0.CO;2-Q.
[42] L. Legras, M.L. Lescoat, S. Jublot-Leclerc, A. Gentils, Optimisation of TEM preparation in metallic materials using low voltage ions, in: European Microscopy Society (Ed.), European Microscopy Congress 2016: Proceedings, Wiley, 2016: pp. 443–444. https://doi.org/10.1002/9783527808465.EMC2016.5973.
[43] P. Xiu, H. Bei, Y. Zhang, L. Wang, K.G. Field, STEM characterization of dislocation loops in irradiated FCC alloys, J. Nucl. Mater. 544 (2021) 152658, https://doi.org/10.1016/j.jnucmat.2020.152658.
[44] Y. Zhu, C. Ophus, M.B. Toloczko, D.J. Edwards, Towards bend-contour-free dislocation imaging via diffraction contrast STEM, Ultramicroscopy 193 (2018) 12–23, https://doi.org/10.1016/j.ultramic.2018.06.001.
[45] A.A. Kohnert, H. Tummala, R.A. Lebensohn, C.N. Tomé, L. Capolungo, On the use of transmission electron microscopy to quantify dislocation densities in bulk metals, Scr Mater. 178 (2020) 161–165, https://doi.org/10.1016/j.scriptamat.2019.11.011.
[46] T. Ungár, P. Frankel, G. Ribárik, C.P. Race, M. Preuss, Size-distribution of irradiation-induced dislocation-loops in materials used in the nuclear industry, J. Nucl. Mater. 550 (2021) 152945, https://doi.org/10.1016/j.jnucmat.2021.152945.
[47] M. Kirk, X. Yi, M. Jenkins, Characterization of irradiation defect structures and densities by transmission electron microscopy, J. Mater. Res. 30 (2015) 1195–1201, https://doi.org/10.1557/jmr.2015.19.
[48] W.C. Oliver, G.M. Pharr, An improved technique for determining hardness and elastic modulus using load and displacement sensing indentation experiments, J. Mater. Res. 7 (1992) 1564–1583, https://doi.org/10.1557/JMR.1992.1564.
[49] J. England, M.J. Uddin, E. Ramirez-Cedillo, D. Karunarathne, S. Nasrazadani, T. D. Golden, H.R. Siller, Nanoindentation hardness and corrosion studies of additively manufactured 316L stainless steel, J. Mater. Eng. Perform. 31 (2022) 6795–6805, https://doi.org/10.1007/s11665-022-06703-w.
[50] H. Pelletier, D. Müller, P. Mille, A. Cornet, J.J. Grob, Dose effect on mechanical properties of high-energy nitrogen implanted 316L stainless steel, Surf. Coat. Technol. 151–152 (2002) 377–382, https://doi.org/10.1016/S0257-8972(01)01596-1.
[51] A. Zaborowska, Ł. Kurpaska, E. Wyszkowska, M. Clozel, M. Vanazzi, F. Di Fonzo, M. Turek, I. Jóźwik, A. Kosińska, J. Jagielski, Influence of ion irradiation on the

nanomechanical properties of thin alumina coatings deposited on 316L SS by PLD, Surf. Coat. Technol. 386 (2020) 125491, https://doi.org/10.1016/j.surfcoat.2020.125491.
[52] M. Saleh, Z. Zaidi, M. Ionescu, C. Hurt, K. Short, J. Daniels, P. Munroe, L. Edwards, D. Bhattacharyya, Relationship between damage and hardness profiles in ion irradiated SS316 using nanoindentation – Experiments and modelling, Int. J. Plast. 86 (2016) 151–169, https://doi.org/10.1016/j.ijplas.2016.08.006.
[53] W.D. Nix, H. Gao, Indentation size effects in crystalline materials: a law for strain gradient plasticity, J. Mech. Phys. Solids 46 (1998) 411–425, https://doi.org/10.1016/S0022-5096(97)00086-0.
[54] A. Kareer, A. Prasitthipayong, D. Krumwiede, D.M. Collins, P. Hosemann, S. G. Roberts, An analytical method to extract irradiation hardening from nanoindentation hardness-depth curves, J. Nucl. Mater. 498 (2018) 274–281, https://doi.org/10.1016/j.jnucmat.2017.10.049.
[55] D. Tabor, The Hardness of Metals, Oxford University Press, 2000.
[56] A. Leitner, V. Maier-Kiener, D. Kiener, Dynamic nanoindentation testing: is there an influence on a material's hardness? Mater. Res. Lett. 5 (2017) 486–493, https://doi.org/10.1080/21663831.2017.1331384.
[57] N. Almirall, P.B. Wells, T. Yamamoto, G.R. Odette, Irradiation microstructures and hardening in commercial nuclear reactor pressure vessel steels at high extended life fluence, Materialia 34 (2024) 102056, https://doi.org/10.1016/j.mtla.2024.102056.
[58] M. Godec, S. Zaefferer, B. Podgornik, M. Šinko, E. Tchernychova, Quantitative multiscale correlative microstructure analysis of Additive Manufacturing of stainless steel 316L processed by selective laser melting, Mater. Charact. 160 (2020), https://doi.org/10.1016/j.matchar.2019.110074.
[59] K.M. Bertsch, G. Meric de Bellefon, B. Kuehl, D.J. Thoma, Origin of dislocation structures in an additively manufactured austenitic stainless steel 316L, Acta Mater. 199 (2020) 19–33, https://doi.org/10.1016/j.actamat.2020.07.063.
[60] A.J. Birnbaum, J.C. Steuben, E.J. Barrick, A.P. Iliopoulos, J.G. Michopoulos, Intrinsic strain aging, Σ3 boundaries, and origins of cellular substructure in additively manufactured 316L, Additive Manufacturing 29 (2019), https://doi.org/10.1016/j.addma.2019.100784.
[61] K. Nordlund, S.J. Zinkle, A.E. Sand, F. Granberg, R.S. Averback, R.E. Stoller, T. Suzudo, L. Malerba, F. Banhart, W.J. Weber, F. Willaime, S.L. Dudarev, D. Simeone, Primary radiation damage: a review of current understanding and models, J. Nucl. Mater. 512 (2018) 450–479, https://doi.org/10.1016/j.jnucmat.2018.10.027.
[62] X. Yi, A.E. Sand, D.R. Mason, M.A. Kirk, S.G. Roberts, K. Nordlund, S.L. Dudarev, Direct observation of size scaling and elastic interaction between nano-scale defects in collision cascades, EPL 110 (2015) 36001, https://doi.org/10.1209/0295-5075/110/36001.
[63] Y. Katoh, R.E. Stoller, Y. Kohno, A. Kohyama, The influence of He/dpa ratio and displacement rate on microstructural evolution: a comparison of theory and experiment, J. Nucl. Mater. 210 (1994) 290–302, https://doi.org/10.1016/0022-3115(94)90183-X.
[64] H.H. Jin, E. Ko, S. Lim, J. Kwon, Effects of helium and hydrogen on radiation-induced microstructural changes in austenitic stainless steel, Nucl. Instrum. Methods Phys. Res. Sect. B 359 (2015) 69–74, https://doi.org/10.1016/j.nimb.2015.07.086.
[65] D. Huan, Y. Li, X. Chen, H. Liu, Effects of fe11+ ions irradiation on the microstructure and performance of selective laser melted 316L austenitic stainless steels, Metals 10 (2020) 1–12, https://doi.org/10.3390/met10091140.
[66] S. Rouland, B. Radiguet, P. Pareige, Investigating radiation-induced segregation on intragranular defects in a 316L(N), J. Nucl. Mater. 557 (2021) 153216, https://doi.org/10.1016/j.jnucmat.2021.153216.
[67] D. Chen, K. Murakami, K. Dohi, K. Nishida, L. Chen, Z. Li, N. Sekimura, Formation of Ni–Si clusters and their relationship with dislocation loops in irradiated stainless steels, J. Nucl. Mater. 578 (2023) 154366, https://doi.org/10.1016/j.jnucmat.2023.154366.